Efficient jib-mainsail fluid-structure interaction modelling – Validations with semi-rigid sails experiments

Antoine Morvan, Matthieu Sacher, Alain Nême, Jean-Baptiste Leroux, Christian Jochum, Nicolas Abiven

▶ **To cite this version:**

Antoine Morvan, Matthieu Sacher, Alain Nême, Jean-Baptiste Leroux, Christian Jochum, et al.. Efficient jib-mainsail fluid-structure interaction modelling – Validations with semi-rigid sails experiments. Ocean Engineering, 2022, 243, pp.110210. 10.1016/j.oceaneng.2021.110210 . hal-03467731

HAL Id: hal-03467731

https://ensta-bretagne.hal.science/hal-03467731

Submitted on 18 Jan 2022

HAL is a multi-disciplinary open access archive for the deposit and dissemination of scientific research documents, whether they are published or not. The documents may come from teaching and research institutions in France or abroad, or from public or private research centers.

L'archive ouverte pluridisciplinaire **HAL**, est destinée au dépôt et à la diffusion de documents scientifiques de niveau recherche, publiés ou non, émanant des établissements d'enseignement et de recherche français ou étrangers, des laboratoires publics ou privés.

EFFICIENT JIB-MAINSAIL FLUID-STRUCTURE INTERACTION MODELLING BASED ON AN EXTENDED *LIFTING-LINE THEORY* – VALIDATIONS WITH SEMI-RIGID SAILS EXPERIMENTS

Antoine Morvan[1], antoine.morvan@ensta-bretagne.org, Matthieu Sacher[1], matthieu.sacher@ensta-bretagne.fr
Alain Nême[1], alain.neme@ensta-bretagne.fr, Jean-Baptiste Leroux[1], jean-baptiste.leroux@ensta-bretagne.fr
Christian Jochum[1], christian.jochum@ensta-bretagne.fr, Nicolas Abiven[2], Nicolas.Abiven@chantiers-atlantique.com

Abstract. The present work takes place in the framework of the "Jib Sea" project. The main purpose of the project is to develop a new sail design made of articulated composite panels, for large merchant ships. The French laboratory "ENSTA Bretagne, IRDL" is involved in this industrial project to provide its expertise on fluid-structure interactions modelling. A fast and robust approach to model fluid-structure interactions for yacht sails is presented. Specifically, interaction effects between the jib and the mainsail are taken into account in the flow model presented. This is achieved using the lifting-line theory combined with a discrete vortex method, involving distributions of lumped-vortex elements along sail sections. The flow model is coupled with a structural finite element software, using shell elements for the modelling of sail membranes, beam stringers for battens modelling and a quasi-static resolution based on a dynamic backward Euler scheme. Numerical comparisons with experiments are conducted on a 50 m² composite mainsail prototype and a conventional jib , built and hoisted on an onshore balestron rig. Measurements, such as strain gauges or cable tensions, are synchronized with a wind sensor. These data collected together enable both global and local numerical-experimental comparisons for forces and moments, providing a validation of the proposed fluid-structure interactions modelling of yacht sails. A good matching between experimental and numerical modelling is observed on local comparisons. Indeed, relative differences are all less than 25% for $TWA \in [-20; 20]$ and $TWS < 10$ kn. Global comparison results exhibit validations with experiments for $|TWA| < 10$ deg and $TWS < 10$ kn, where numerical-experimental relative differences are less than 10%.

1. NOMENCLATURE

C_{var}	Variation coefficient $[-]$
c	Chord length $[m]$
ds	Integration element $[m]$
e	Euler number $[-]$
F	Force $[N]$
h	Batten height $[m]$
i	Imaginary number $[-]$
j, k	Index $[-]$
L	Length $[m]$
M	Moment $[N.m]$
N	Number of element $[-]$
Q	Element for DVM $[-]$
U	Wind velocities $[m.s^{-1}]$
V	Flow velocities $[m.s^{-1}]$
w	Complex velocity $[m.s^{-1}]$
$\mathcal{Z}$	Complex number $[-]$
α	Angle for LLT $[deg]$
Γ	Global circulation $[m^2.s^{-1}]$
γ	Local vortex circulation $[m^2.s^{-1}]$
ΔP	Pressure variation $[Pa.]$
Δl	Elongation $[m]$
ε	Relative error $[-]$
θ	Local angle per element $[deg]$
μ	Mean $[N]$ or $[N.m]$
σ	Standard deviation $[N]$ or $[N.m]$
ρ_0	Density $[kg.m^{-3}]$
ω_i	Induced velocity $[m.s^{-1}]$
$\langle EI \rangle$	Out-of-plane bending stiffness $[N.mm^2]$
LE	Leading edge
TE	Trailing edge
x, y, z	Spatial coordinates $[m]$

2. INTRODUCTION

The present work is part of a substantial industrial project, called "Jib Sea", bringing together several industrial companies and ENSTA Bretagne as the academic partner. The main purpose of this project is to develop new rigid sails for use on large merchant ships. Such sails are made of composite panels that hoist and lower like an accordion. The main benefit of this kind of articulated composite sails stays in the increase of the lifetime, and the possibility to significantly increase sail areas to face values of more than 1000 m^2.

The ENSTA Bretagne laboratory is involved in this industrial project to provide its expertise on Fluid-Structure Interactions (FSI) modelling. In most cases, sails are manufactured with thin textile fibers [1]. The aerodynamic loading on thin sail membranes usually involves large displacements and deformations [2], that directly affect the flying shape of the sail and consequently pressure fields. It is therefore necessary to consider a nonlinear coupled approach to correctly capture the sail FSI phenomenon [3]. However, because of the complex coupled aero-elastic behaviour of yacht sails, nonlinear FSI computations are rather difficult to implement. Furthermore, the modelling strategy must be able to couple both structure and flow solvers.

[1] ENSTA Bretagne, CNRS UMR 6027, 2 Rue François Verny, F29200 Brest, France
[2] Chantiers de l'Atlantique, Avenue Antoine Bourdelle, F44600 Saint-Nazaire

In most of cases, structure solvers are based on discretized method, such as the well-known Finite Element Method (FEM). For flow solvers, resolution methods are usually based on viscous or inviscid flow models [4]. The fairly simple implementation and the fast computation time of inviscid models makes them very popular and used today. Viscous flow approaches start also to be used, but they are usually limited to large industrial projects with adequate time and money. In most of industrial projects, these computations are still very expensive, in addition to convergence or mesh deformation problems that may happen. Consequently, there is a real need nowadays for the design departments of yacht companies to work with fast and robust FSI solvers, allowing a fast and easy to use accurate enough modelling.

The FSI computation approach of the present paper follows a strategy very similar to the work of Sacher et al. [5]. However, the method is extended to the flow solver part. Especially, the proposed flow model considers now interaction effects between jib and mainsail. The structural and flow solvers, respectively FEM and Lifting-Line Theory (LLT), are the same, considering a steady solution of the nonlinear FSI problem. The LLT model from the Prandtl [6] theory is applied as in [5], but pressure fields are now computed using the Discrete Vortex Method (DVM) from Katz and Plotkin [7]. The structural solver part of, the presented method is performed using *Abaqus™ 2017* finite element software. As in [5], a quasi-static approach is involved with a dynamic backward *Euler* scheme [8] to improve the convergence robustness using a standard *Newton-Raphson* method. The mainsail membrane and the reinforcements are modelled with shell elements, battens are modelled with stringers elements connected to shell nodes. The cables connecting the panels are modelled with spring connecters. Each panel luff is pinned to the mast and is free to move along it. In order to simplify the FSI problem, the solving of the jib structure response was not conducted even if it could have been considered by the strategy presented in this work. However, the jib was modelled from an aerodynamic point of view based on a rigid geometry assumption to be considered in the flow solver.

Numerical comparisons with experiments are furthermore provided in the second part of this work. As for experimental setup ,a 50 m² composite mainsail prototype and a conventional jib have been built and hoisted on an onshore balestron rig (see Figure 1) to provide several measurements, such as strain gauges or cable tensions, synchronized with a wind sensor. These data collected together enable both local and global numerical-experimental comparisons, to validate the proposed FSI modelling of yacht sails.

In the following, Section 3 of the paper outlines the FSI modelling strategy proposed. Section 4 presents the composite mainsail prototype and its dedicated sensors. In Section 5, numerical to experimental comparisons on the composite mainsail prototype are presented and results observed allow a reasonable validation of the sail FSI modelling strategy. Finally, main conclusions on this work are given in Section 6.

Figure 1 Jib Sea prototype at 1:5 scale.

3. NUMERICAL MODEL

Compared with a previous work [5], where only the mainsail was considered, the present study is extended to account for the jib. In this work, the mast is still considered rigid and we assume that the FSI problem has a steady solution, which allows to couple flow and structural solvers with a quasi-static approach.
In the following, the flow and the structural solver are respectively described in Part 3.1 and Part 3.2. Part 3.3 presents the FSI coupling technique and Part 3.4 summarizes the major uncertainties and modelling strategies.

3.1. Aerodynamic Models

In this part, the flow model for wind aerodynamic loads on sails is derived.
As a hypothesis, we consider that the wind acting on sails can be modelled by an inviscid flow. Paragraph 3.1(a) provides details on the computation, of flow characteristics on sails along the span (mainsail and jib), based on the *Lifting-Line Theory* modelling approach. Paragraph 3.2(b) describes the calculation of the aerodynamic pressure fields along the chord of the mainsail and the jib, using the *Discrete Vortex Method*.

3.1(a) Flow characteristics

Using the *Lifting Line Theory* (LLT) and similarly to Sacher et al. [5] the two sails are modelled as a single straight lifting line and an associated vortex sheet. The main difference with [5] is that here the sections are composite, as being made up of two sub-sections: one for the jib and one for the mainsail. This is illustrated in Figure 2, considering at a given z coordinate a two-dimensional (2D) section subjected to a uniform flow $\vec{U}_0$ of angle α with the x-axis defined by the lifting sections of the jib and the mainsail of chord lengths $c_{jib}(z)$ et $c_{main}(z)$:

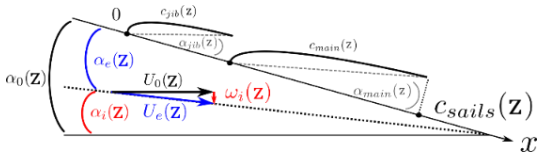

Figure 2 Induced velocity and induced angle in the vicinity of the composite section of the lifting line model.

The LLT allows to compute the induced velocity field along the span, $\omega_i(z)$ and $\alpha_i(z)$, as defined in Figure 2 (see references [5], [6], [7]). The effective angle $\alpha_e(z)$ and the effective velocity $U_e(z)$ of the flow at a given height z are then obtained, according to equations (1):

$$\begin{cases} \alpha_e(z) = \alpha(z) - \alpha_i(z) \\ U_e(z) = U_0(z) + \omega_i(z) \end{cases} \quad (1)$$

In the following, aerodynamic pressure fields along the sails chord are computed section by section using $\alpha_e(z)$ and $U_e(z)$

3.1(b) Aerodynamic pressure field

The LLT method alone cannot compute local aerodynamic sail pressure loads, but provides chord- integrated loads along the span. An additional aerodynamic formulation is required for this purpose. In the previous work [5], a semi-analytical model from the well-known linearized thin wing sections theory was used. In this work, it has been replaced by the use of the *Discrete Vortex Method* (DVM) [7], more suitable to deal with two-element sections. Considering at a given z coordinate, the section (jib + mainsail), in the effective velocity field $(U_e(z),\ \alpha_e(z))$ calculated from the LLT, the DVM allows to model the lifting potential flow subjected to the boundary conditions $(2.a)$ and $(2.b)$:

$$\begin{cases} \vec{V}_{jib}.\vec{n}_{jib}|_{L_{jib}} = 0 \ and \ \vec{V}_{main}.\vec{n}_{main}|_{L_{main}} = 0 & (2.a) \\ \Delta P|_{TE_{jib}} = 0 \ and \ \Delta P|_{TE_{main}} = 0 & (2.b) \end{cases}$$

The circulation Γ, defined in equation (3), where $\vec{V}_{jib}$ and $\vec{V}_{main}$ are respectively the flow velocity around the jib and the mainsail section, is generated using a discrete vortex distribution.

$$\Gamma = \oint_{L^-_{jib} \cup L^+_{jib}} \vec{V}_{jib}.\vec{t}_{jib} ds + \oint_{L^-_{main} \cup L^+_{main}} \vec{V}_{main}.\vec{t}_{main} ds \quad (3)$$

The two-element lifting section is discretised into N elementary facets $[Q_{k-1}, Q_k]$ of length ds_k (see Figure 3).

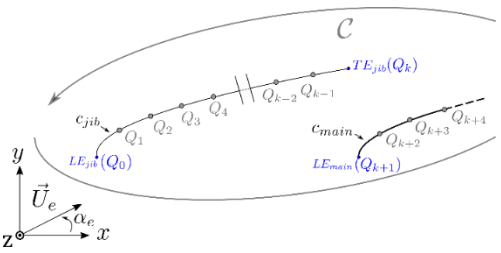

Figure 3 Two-element lifting section discretization. Here only a focus on the jib section has been represented.

The number of N elementary facets is about 2500. The circulation contribution of each ds_k facet is modelled by a discrete vortex of intensity γ_k located at one quarter of the leading edge of the facets.The flow tangency boundary condition is applied at one quarter of its trailing edge (see Figure 4 and [7]).

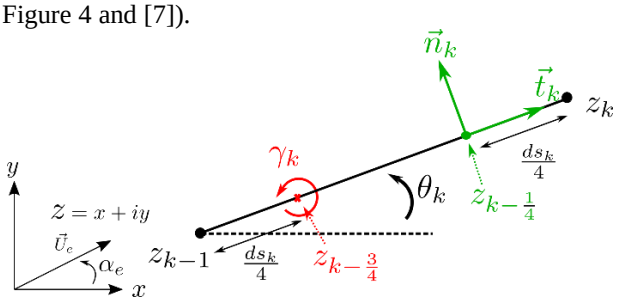

Figure 4 Local parametrization of a ds_k facet.

For each section, the flow tangency boundary condition (4) is expressed in the complex number space as presented in equation (5):

$$Im\left[w_{j-\frac{1}{4}} e^{i\theta_j}\right] = 0 \quad (4)$$

Where:

$$w_{j-\frac{1}{4}} = U_e e^{-i\alpha_e} - \sum_{k=1}^{N_{jib}} \frac{i\gamma_k}{2\pi\left(Z_{j-\frac{1}{4}} - Z_{k-\frac{3}{4}}\right)} - \sum_{k=1}^{N_{main}} \frac{i\gamma_k}{2\pi\left(Z_{j-\frac{1}{4}} - Z_{k-\frac{3}{4}}\right)} \quad (5)$$

Three-dimensional effects being considered through the couple $(\alpha_e(z), U_e(z))$ computed by the LLT.
The writing of the $N = N_{jib} + N_{main}$ flow tangency boundary condition leads to a system of N linear equations for the N unknowns sγ_k. The solving of this linear system provides all vortex intensity γ_k per lumped-vortex elements for the jib and the mainsail.
Finally, for each element of the discretisation of the jib and mainsail section, the pressure load (6) is approximated constant per element from the Kutta formula:

$$\Delta P_k = -\frac{\rho_0 U_e \gamma_k}{ds_k} \quad (6)$$

The FSI coupling strategy is presented.in following Part 3.2 and Part 3.3,

3.2. Structure model

The structure modelling approach is performed using the *Abaqus*™ finite element analysis software and is based on a discretisation of the mainsail only, by means of several finite element panels. Main leech and luff connections between the 12 mainsail panels are modelled with nonlinear spring elements, having following stiffness law:

$$F = 6310\Delta l^{1.19} \quad (7)$$

This stiffness law has been determined from experiments, where F denotes the tension in the loop in Newton and Δl the corresponding elongation in millimetres. The secondary connections between panels along the battens are modelled with two-dimensional linear spring connections.

Sail battens are modelled with equivalent beam stringer elements “B33” and “STRI3” shell *Kirchhoff* elements are used for the modelling of thin composite panel membranes (see Figure 5). For more information, the reader may refer to the *Abaqus*™ User’s Manuel [9]. The whole number of shell element at mesh convergence is about 200 000 [5].

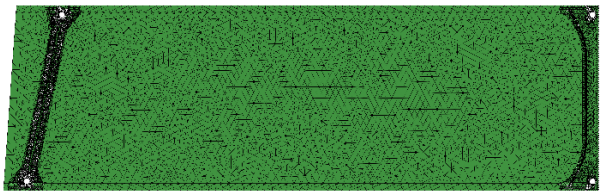

Figure 5 GP1 panel mesh.

Structural computations of thin sail membranes are often complex because of buckling issues due to possible appearance of wrinkles. In this work, respectively shell *Kirchhoff* elements and beam *Euler-Bernoulli* elements are suitable for thin plate and slender rod, since they are not subjected to transverse shear locking phenomena. A specific shell thickness approach is presently implemented [5] to catch sail extension deformations by neglecting small wrinkles. Each panel consists of glass-epoxy membranes and carbon-epoxy reinforcements. The classical laminate theory [10] is applied for the behaviour of the shell *Kirchhoff* elements. Note that the jib structure is not presently computed. Many tied contacts have been introduced in the finite element model to reproduce the bonding between the reinforcement parts (see Figure 6).

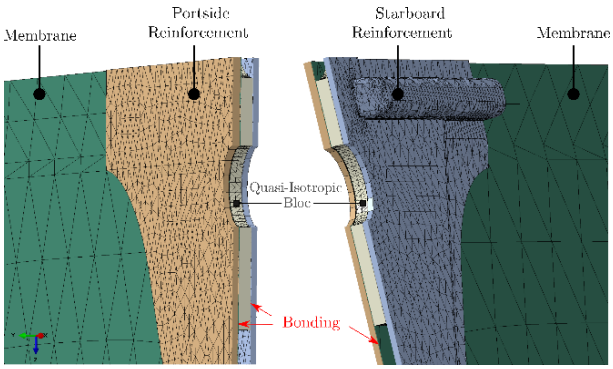

Figure 6 Assembly of bonded parts.

3.3. FSI Coupled Problem

The nonlinear problem solving is performed with a specific quasi-static resolution based on a dynamic backward *Euler* scheme [5]. The jib is considered from an aerodynamic point of view. Consequently, aerodynamic pressure on mainsail is computed according to the presence of the jib (see Part 3.1). In that way, the jib acts as a flow disturbance seen by the mainsail, and an example of mainsail pressure field, with and without jib showing jib effects, is given in Figure 7. After a *Delaunay* triangulation of the sails (Figure 8), the aerodynamic pressure field is applied on each mainsail structural shell element centroids by using bi-linear interpolations with *Lagrange* polynomials.

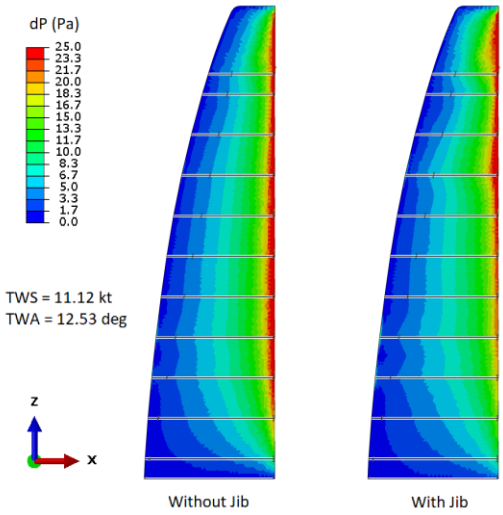

Figure 7 Pressure field on the mainsail with (left) and without (right) jib.

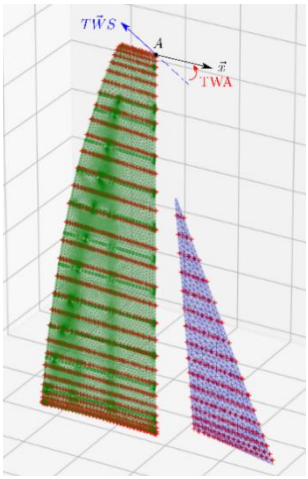

Figure 8 Delaunay mesh triangulation.

An overview of the FSI coupling algorithm scheme is presented in Figure 9

input : Non-deformed structural mainsail mesh
output : Deformed and loaded mainsail mesh
compute # Mainsail and Jib pretension
 # FSI main loop
while Not Converged do
- ***# Fluid solving***
- **compute #** LLT
  - Delaunay triangulation of structural mesh
  - Sail sections along $\vec{z}$ using $(\vec{x}, \vec{y})$ plane intersections with triangulation
  - From $U_0(z)$ and $\alpha(z)$ solve Prandtl equation see Sacher et al. [5] and Katz and Plotkin [7]
  - Use Equation (1) to get $U_e(z)$ and $\alpha_e(z)$
- **compute #** Pressure loads DVM
  - From $U_e(z)$ and $\alpha_e(z)$ linear system implementation through Equation (4)
  - $\gamma(x)$ on each mainsail and jib section with (5)
  - $\Delta P(x)$ on each mainsail section with (6)
  - Bi-linear interpolations of ΔP on structural shell element centroids
- ***# Structure solving → compute Abaqus ™***

Figure 9 FSI Algorithm.

An example of nonlinear FSI results is provided in Figure 10, where the transverse (y-axis direction) mainsail displacement $[m]$ is illustrated with colored contours.

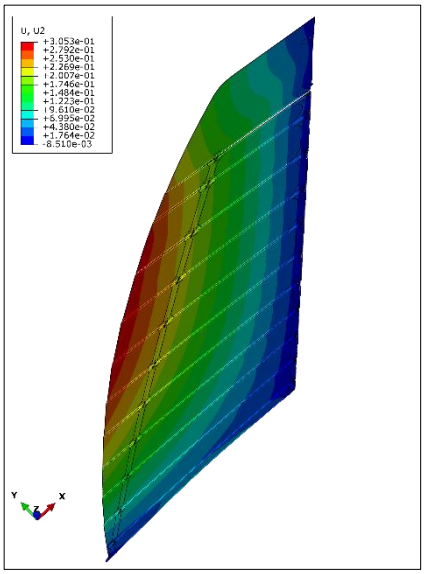

Figure 10 Example of FSI results.

3.4. Numerical uncertainties and investigations

Part 3.4 gathers several important remarks related to the development of the numerical model and exposes relevant strategies to solve modelling issues.

The question of the meshes convergence is not presented in this work. To determine the accurate mesh size, the previous study [5], which contains a study of meshes convergence onto a similar semi-rigid sail, is used. The accurate average size of elements has been scaled for the "Jib Sea" sails and set to 0.125m.

The stopping criterion of the FSI calculation presented in Figure 9 is reached as soon as relative differences between consecutive iterations of several relevant mechanical parameters is below a fixed threshold. The threshold is set at 10^{-4} for following mechanical parameters: mainsheet load, cunningham load, halyard load, side force, global strain energy and maximum displacement. In practice, the FSI calculation converges after six iterations.

To validate the structural numerical model and the calculation process, an experimental study on GP5 regarding its bending behavior is carried out. Indeed, for a fully modelled panel, the bending behavior of the panel is mainly controlled by the stiffness of the battens (Figure 11).

This study has the aim to investigate the mechanical response of the battens through the height of the carbon epoxy UD part inside of the composite battens section (Figure 13).

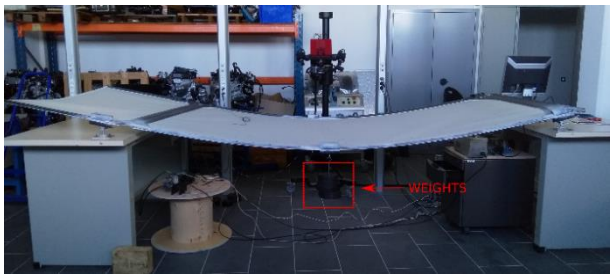

Figure 11 Picture of GP5 panel under loading: 14.26 kg per battens.

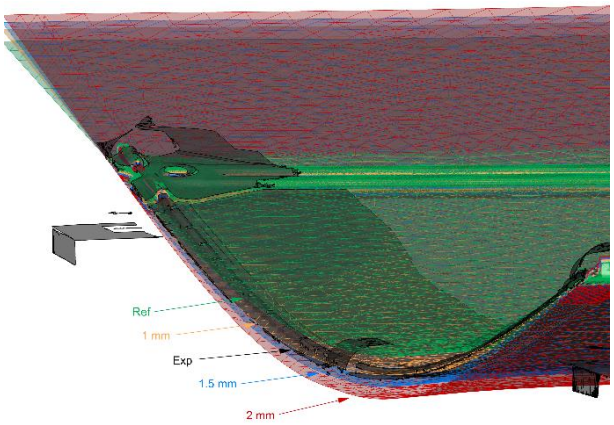

Figure 12 Experimental deflection of the GP5 (Exp) and numerical deflections for 4 carbon UD locations (Ref, $1mm$, 1.5mm and 2mm) under pure bending loading of 28.52 kg.

Figure 12 shows that the experimental deflection of GP5 is between the numerical deflections results respectively for a carbon UD offset of 1mm and 1.5mm. Thus, for all mainsail battens in the numerical model, carbon UD was shifted by 1.5 mm (y-direction) compared to the original geometry of the battens (see Ref from Figure 12).

In a previous work, the structural model of synthetic connectors between panels (i.e. Loop in Figure 18), was a simple axial spring having a stiffness of $10^7 N/m$. A sensibility analysis has been conducted to compare the maximum loop force at the leach when dividing the stiffness by 10 or 100. A division of the axial stiffness by 10 leads to a decrease in force of about 26%, while a division by 100 decreases the force by 61%. According to these observations, an experimental test was carried out on a single loop to characterize the non-linear behavior in terms of force and displacement as shown by equation (7).

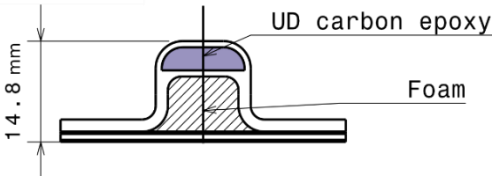

Figure 13 Side view of batten CAD.

4. EXPERIMENTAL SETUP

In this section, the experimental setup of the 1:5 composite mainsail prototype is presented. Part 4.1 deals with the materials used for the manufacture of the prototype, while Part 4.2 presents the sensors that were set on the mainsail prototype. Part 4.3 summarizes relevant uncertainties linked to sensors measurements and highlights important information on sensors uncertainties. Due to financial restrictions, we did not measure the deformation and displacement of the sail. This would have been an additional means of validating the simulations. During the tests, we did not visually encounter any major instability effect, such as membrane large wrinklings , batten buckling or flapping of the sail for instance. We therefore assume the uniqueness of the mechanical solution. Thus, only force or moment measurements allow us to validate the whole numerical model which includes sail deformation. Moreover, force or moment are physical quantities that triger the design of the sail.

4.1. Prototype overview

The 1:5 scale mainsail prototype is made of 12 composite panels connected to each other with textile loops made of "Dyneema SK78", as shown in Figure 16. The mainsail area is about 50 m². The jib of about 13 m² is a classical one made of Hydranet (polyethylene+polyesther) and manufactured by XVOILES. Mainsail membranes are made as a fiberglass composite, having a thickness of about 0.2 mm. The panel reinforcements and battens are manufactured using carbon epoxy laminates

All components of the mainsail are held up on a super-structure called a balestron rig (see Figure 14), which is made of aluminium alloy. The major difference with a standard rig is that there is no boom per se.

Figure 14 Balestron rig full view.

The balestron rig supporting the composite mainsail and the classical jib has been installed onshore at Pornichet in France, and was fitted with a motor allowing it to rotate around the z-axis (vertical axis) of the ground coordinate system.

This feature is very useful to target a true wind angle (TWA) during testing. The TWA is obtained by an anemometer located at the top of the mast as shown in Figure 8. For this configuration, the x-vector is unitary and parallel to the vector connecting the clew of the main sail and the mast foot. TWA is positive when the wind comes from starboard.

4.2. Prototype sensors

The 1:5 scale prototype (see Figure 1) is fitted with several sensors to study the mechanical behaviour of the mainsail under aerodynamic loadings. The jib is not instrumented. The mainsheet, the cunningham and the halyard are fitted with snap hook with load cell sensor (see Figure 15).

(a) (b)

Figure 15 (a) mainsheet load cell sensor (b) cunningham load cell sensor.

Most of the sensors are set on the first large panel, named GP1 as illustrated in Figure 18. A homemade load cell sensor, *LoopBckUp*, is set on the textile loop located at the bottom leech of the GP1 panel (see Figure 16) in order to measure tension forces between the two composite panels, PP1 and GP1.

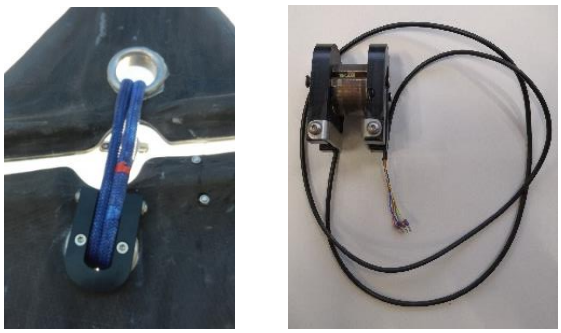

(a) (b)

Figure 16 (a) *LoopBckUp* close-view (b) homemade load cell

The link between the GP1 panel and the rigid mast is instrumented through the luff rail (Figure 18). These rail sensors, called *RailTransver*, are made of strain gauges and are able to measure starboard and portside components of the GP1 forces. Other gauges, called *RailAxial* are installed on the luff rail and are able to measure tension and compression forces generated by GP1 on the mast (see Figure 17).

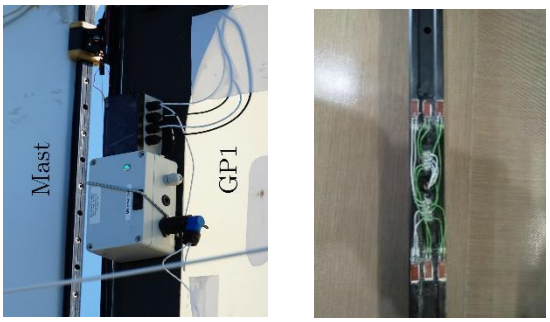

(a) (b)

Figure 17 (a) Instrumented luff rail (b) strain gauges installed on the luff rail.

The battens of GP1 are also instrumented (see Figure 18) to measure the bending moment due to the aerodynamic loading.

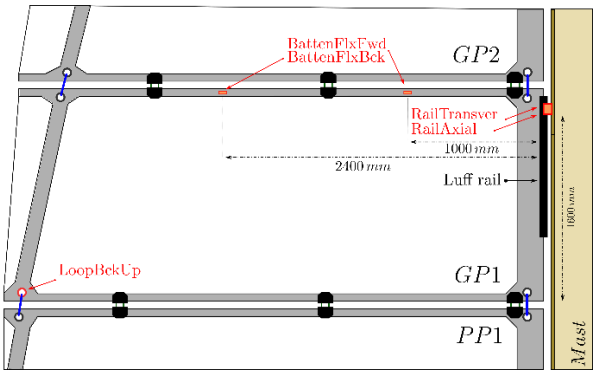

Figure 18 Sketch of the GP1 with sensor locations.

For these measurements, two sets of strain gauges, respectively called *BattenFlxFwd* and *BattenFlxBck*, have been bonded on the upper batten of GP1 (see Figure 18).

4.3. Sensors Uncertainties

The quantification of measurement noise in the data recorded by the sensors was performed when the sails are in the eye of the wind. For the load cells, the highest contribution of noise is about 23 N for the *Halyard*. For the *RailTransver* and *RailAxial*, the contribution of the noise is about 5 N. and for the *BattenFlxFwd* and *BattenFlxBck* less than 1 $N.m$.

The calibration of all the sensors except those of the Rail has been carried out indoor by means of a calibration bench. *RailTransver* and *RailAxial*, sensors calibration was carried out on the prototype using a calibration bench. All data are recorded in real time at a sampling rate of 1Hz and are stored directly in a data control center "onboard".

5. RESULTS: NUMERICAL VS EXPERIMENTAL

Section 5 provides several numerical and experimental results related to the experimental set-up presented in Section 4. The numerical FSI model presented in Section 3 is applied. Two types of experimental vs numerical comparisons are presented. Specifically, Part 5.2 deals with global comparisons based on metamodeling, while Part 5.1 presents local comparisons. All following comparisons are carried out with the jib.

5.1. Local comparisons

In this part numerical to experimental local comparisons results are provided. This type of comparisons consists of comparing experimental data with the corresponding *Abaqus*™ calculations for a specific almost "stable" TWA and TWS aerodynamic loading. Actually, due to the onshore experimental system, it is really challenging to obtain stable wind conditions allowing almost constant sail responses to the loads.

However, a moving average approach, with a six seconds window was implemented and set with a criterion on the variation coefficient.

The acquisition frequency of the sensors is one *Hertz*. This method allows to keep relevant only data where TWA and TWS are nearly stable. The variation coefficient is defined as follows:

$$C_{var} = \frac{\sigma}{|\mu|} \tag{8}$$

Where σ and μ are respectively the standard deviation and the mean of the TWA or the TWS, over a given time period. In practice, a time period is arbitrary defined to be stable if the variation coefficient is less than 15%. Figure 19 shows an example of experimental data, on a selected time period, that is presently used for the following local comparisons.

The decrease of the *Mainsheet* tension, during the selected time period is probably due to the viscoelastic relaxation of the loops. A sensitivity analysis on the simulation results showed that around the average parameters (Eq. 9) a 15% variation of TWS and TWA generates a standard deviation of 52 N on the values of the mainsheet tension. This standard deviation is relatively small compared to the decrease of about 300 N observed in the selected experimental window (Figure 18) and confirms viscoelastic relaxation of the loops..

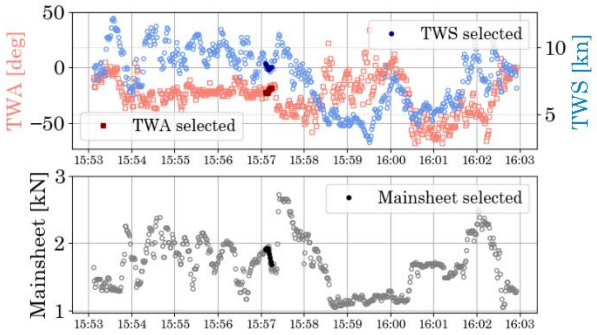

Figure 19 Selected experimental data for local comparisons. TWS and TWA are respectively plotted with blue and red markers. Black markers correspond to the *Mainsheet* tension. Bolded markers represent the stable time period.

The aerodynamic loading is determined by averaging the selected stable time period. In that case (see Figure 19), it leads to following reasonable set:

$$\begin{cases} TWA = -20.76\ [deg] \\ TWS = \quad 8.53\ [kn] \end{cases} \tag{9}$$

Each local experimental quantity (see sensors descriptions in Section 4), to be compared with the *Abaqus*™ computation, is obtained by averaging the almost stable selected time period. The relative difference is used to assess numerical to experimental local comparisons:

$$\varepsilon[\%] = 100 \times \left| \frac{X_c - X_e}{X_e} \right| \tag{10}$$

where X_c and X_e are respectively numerical and experimental quantities to be compared. Bar charts are used to highlight comparisons results. The black item denotes the measurement dispersion at more or less 2σ.
Figure 20 shows that local comparisons for *Mainsheet*, *Cunningham*, *Halyard* and *LoopBckUp* sensors are overall satisfactory.

The highest relative difference is around 25% for the *Halyard*, while all the others are less than 15%. As for measurement dispersion, only the numerical *LoopBckUp* may match the simulation.
For these comparisons, related to the mechanical behaviour of textile fibre ropes, it is not obvious to explain where the differences come from. However, for the *Mainsheet* and the *Cunningham*, numerical to experimental differences can be explained by the mechanical relaxation of the polymer textile fiber.

In the current numerical model, the input pre-tensions of the *Mainsheet* and *Cunningham* are determined with experimental measurements evolving over time. In order to determine input pre-tensions, a linear approximation between 3 points was performed. In order to better determine these input pre-tensions, it would be interesting to use a decreasing exponential [11] approximation.

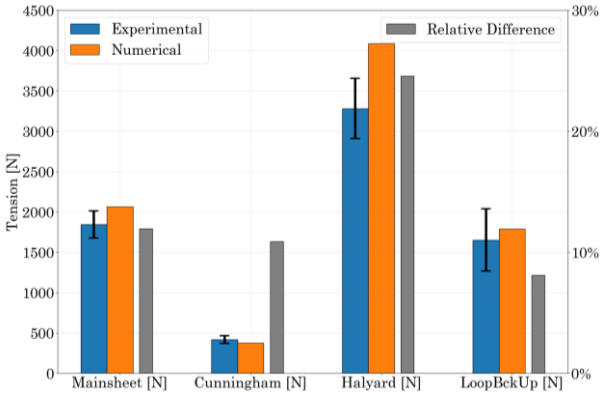

Figure 20 Local comparisons and relative difference for the *Mainsheet*, *Cunningham*, *Halyard* and *LoopBckUp*.

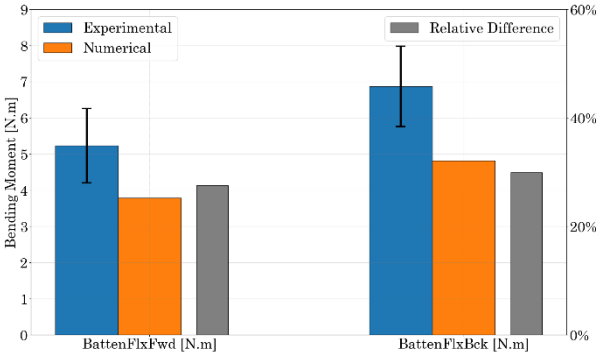

Figure 21 Local comparisons and relative difference for the *BattenFlxFwd* and *BattenFlxBck*.

Figure 21 shows that numerical results underestimate experimental measurements of about 30%. By considering measurement dispersions at $\pm 2\sigma$, for both battens, relative differences drop to 10%. Regarding these last observations, comparisons for battens are not so bad for bending moments. Nevertheless differences might be explained by analyzing the data of the formula used to compute the batten bending moments:

$$M_{ben} = \frac{2\langle EI \rangle}{\kappa h}(x_{mes\ batten} - x_{0\ batten}) \tag{11}$$

Where $\langle EI \rangle$ is the out-of-plane bending stiffness of the batten, h its height and κ the gauge factor.

Some discrepancies may subsist between the real value of $\langle EI \rangle$ and h from the manufacturing and the theoretical numerical value set in the FEM *Abaqus*™ model. Moreover, secondary connecting systems between panels along the battens are complex and difficult to model well. Two dimensional linear spring connectors are used. This approach should be improved to obtain a better correlation with experiment regarding bending moment along the batten.

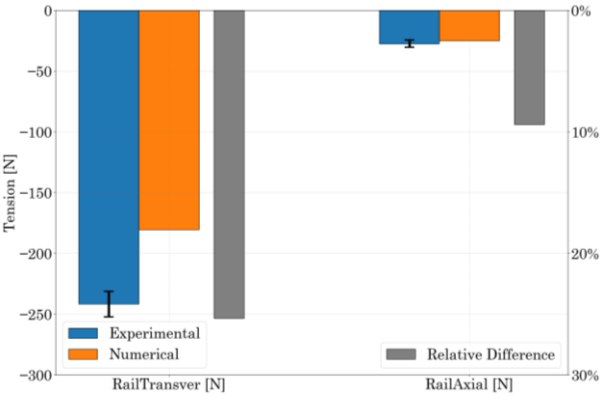

Figure 22 Local comparisons and relative difference for the *RailTransver* and the *RailAxial*.

Figure 22 shows similar results to those in Figure 21. From a magnitude point of view, numerical results underestimate experimental results of about 25% for the *RailTransver* and of about 10% for the *RailAxial*. By estimating measurement dispersions, numerical results can match experimental measurements for the *RailAxial*.

As previously said, improvement of the secondary connecting system modelling should enhance numerical bending behavior of the battens and consequently the transversal reaction force of the mast.

Since the luff rail can undergo a large rotation, a fictive new local coordinate system $(O, \vec{X}_R, \vec{Y}_R, \vec{Z}_R)$ is built from the deformed coordinates of points HR, LR and MC (see Figure 23).

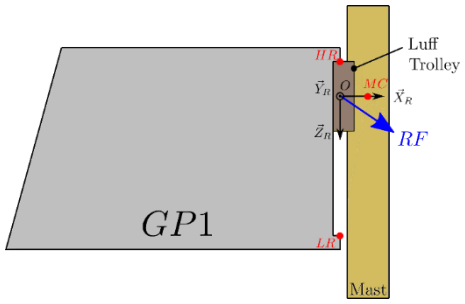

Figure 23 Sketch of the new local coordinates system

Afterwards, in order to perform comparisons with experimental sensors measurements, *Abaqus*™ output results for the rail, as vector $\overrightarrow{RF}$, at point O is projected along vector $\vec{X}_R$ for the *RailAxial* and along $\vec{Y}_R$ for the *RailTransver*. Consequently, differences may come from the projection of $\overrightarrow{RF}$ along $\vec{X}_R$ and $\vec{Y}_R$ through the building of the fictive local coordinates system. Because the mast is considered as rigid, coordinates of MC are unchanged after the aerodynamic loading contrary to the point HR and LR.

5.2. Global comparisons

Global comparisons were carried out in three steps. Firstly, to compare experimental data collected by a single sensor with numerical results for a wide range of *TWS* and *TWA*. In this way, two 3D scatter plots are superimposed: denoting respectively experimental data and numerical results. Secondly, based on these two scatter plots, two response surfaces are computed using a *Gaussian processes* [12]. Thirdly, in order to quantify more precisely differences between numerical results and experimental measurements, coloured "iso-contours" plots are used. Differences between numerical and experimental response surfaces are then analysed to validate the proposed numerical modelling of sails FSI. This numerical to experimental comparison allows a validation of the numerical FSI model in terms of trend and relative differences on a large range of sails operating points. This three-step process was carried out for the *Mainsheet*, the *RailTransver* and the *BattenFlxBck*.

Figure 24 shows numerical and experimental response surfaces of the $Mainsheet$ tension in $[N]$. It can be noticed that the numerical model (*blue*) overestimates the measurements (red) for large values of $|TWA|$. However, for $TWA \in [-10; 10]$ deg, the numerical model response almost fits the experiments.

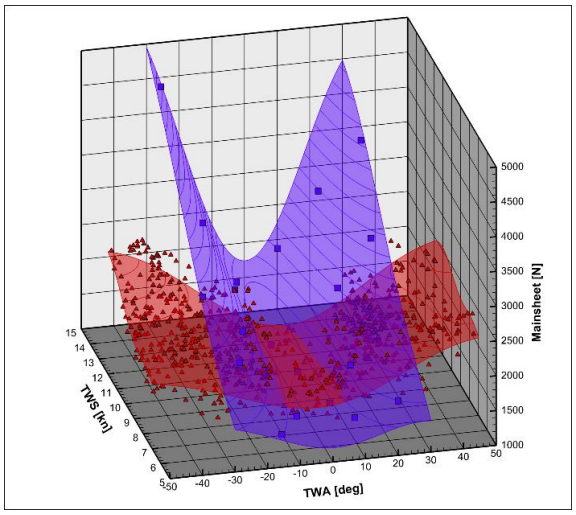

Figure 24 Experimental (red) and numerical (blue) response surfaces of the *Mainsheet tension* built from experimental measurements (red triangles) and numerical results (blue squares).

Figure 25, where relative differences between numerical and experimental responses are shown, confirms the observations made in Figure 24. Relative differences are less than 5% for $TWA \in [-10; 10]$ deg. It should be noted that even for large $TWA \in [-20; 20]$, relative differences remain less than 25% for $TWS < 10$ kn. These observations are in accordance with the limits of an inviscid flow model, which computes an attached sail flow and therefore overestimates sail forces for large TWA values.

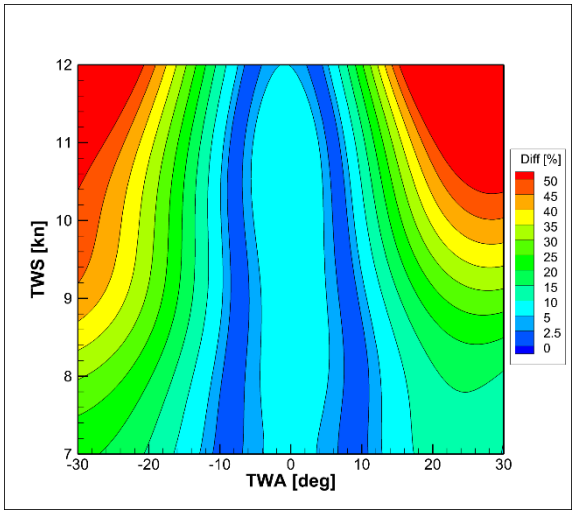

Figure 25 Relative difference between experimental and numerical results for the *Mainsheet* tension.

Figure 26 shows numerical and experimental response surfaces of the bending moment in the $BattenFlxBck$. Response surfaces are very close for $TWS < 10$ kn, while for large TWS values, the numerical model seems to overestimate the experiments. This trend is confirmed by absolute differences of response surfaces that are provided in Figure 27. Absolute differences of the bending moment appear to be less than 1.5 N.m for $TWS < 10$ kn.

Regarding experimental values of the bending moment, relative numerical to experimental differences are about 5 to 10%. Higher absolute differences can be observed for a starboard loading when TWS is greater than 11 kn and 25 deg. of TWA. This asymmetrical response of the batten bending moment regarding the TWA comes from its starboard to portside asymmetrical mechanical properties as battens are located on the starboard side of the panel. Comparing the $Mainsheet$ tensions, differences observed here between numerical predictions and measurements are less pronounced for large TWA. This may be explained by the fact that at low or moderate TWS, the GP1 panel is lightly loaded.

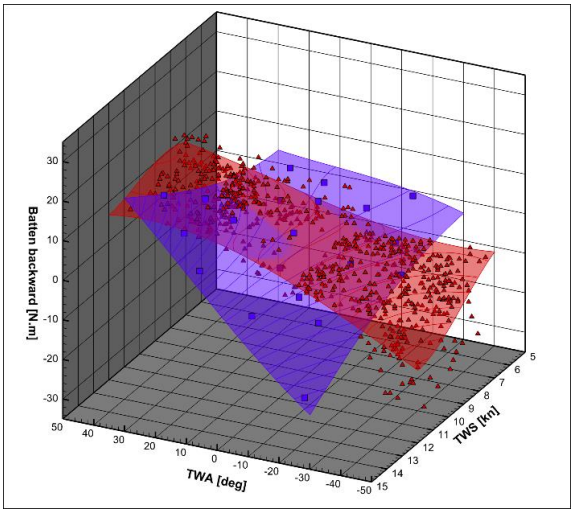

Figure 26 Experimental (red) and numerical (blue) response surfaces of the bending moment in *BattenFlxBck* built from experimental measurements (red triangles) and numerical (blue squares).

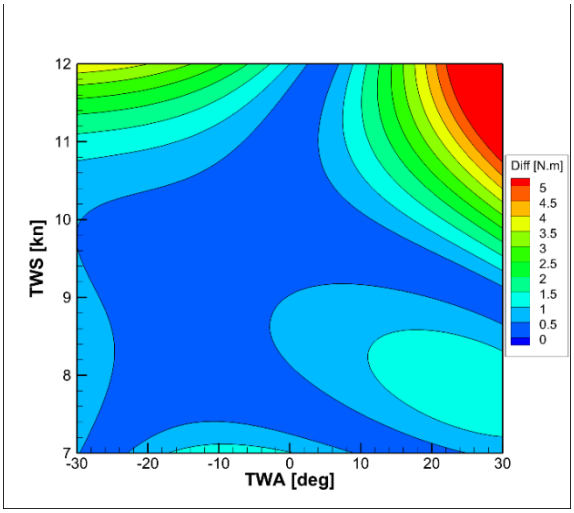

Figure 27 Absolute difference between experimental and numerical results for the *BattenFlxBck* moment.

Figure 28 is related to the force in the $RailTransver$, and is similar to results provided in Figure 26. For the common $[TWA, TWS]$ range both response surfaces are evolved in the same way and seem to be very close. Figure 29 confirms that both response surfaces are evolving in the same way within $3/4$ of their common $[TWS, TWA]$ pair. In this area the absolute difference is less than 6 N, that corresponds to relative differences of again 5 to 10%.

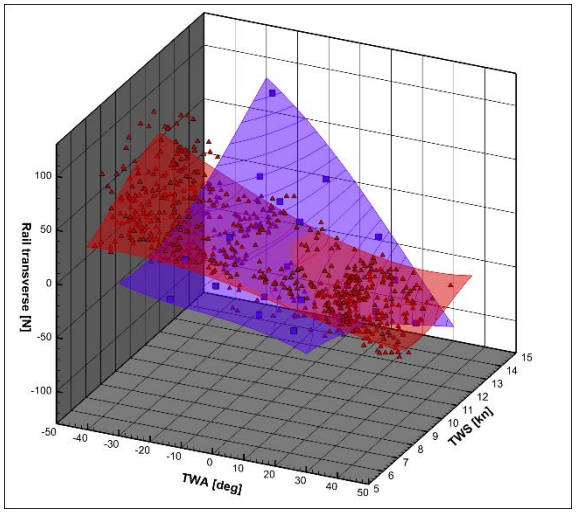

Figure 28 Experimental (red) and numerical (blue) response surfaces of the force in *RailTransver* built from experimental measurements (red triangles) and numerical (blue squares).

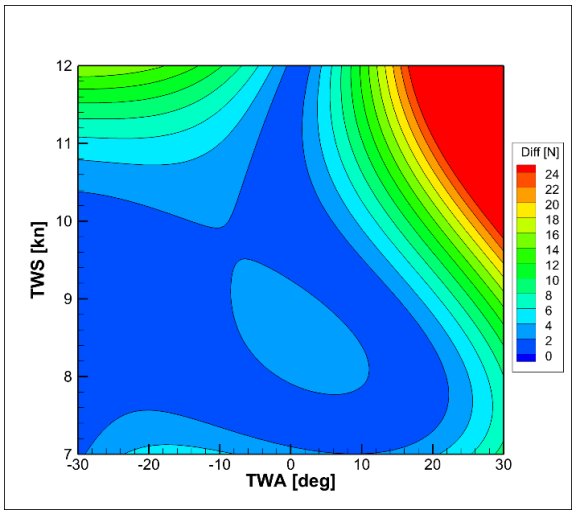

Figure 29 Absolute difference between experimental and numerical results for the *RailTransver* force.

According to these last observations and more specifically numerical to experimental differences, it has been shown that numerical FSI results are very close to the experiments for moderate values of TWA. This is particularly true for the $Mainsheet$ tension that is directly related to the global mainsail lift force. As already mentioned, this overestimation of the mainsail lift for large TWA is explained by the limits of the presently implemented inviscid flow model, that does not compute possible sail flow separations. Regarding at more local quantities, such as the rail transverse force and the batten bending moment of the GP1 panel, numerical to experimental differences are also increasing for large TWA values, but only for $TWS > 10$ kn.

At low and moderate TWS, the GP1 panel appears to be not enough loaded to see numerical to experimental differences. Nevertheless, it should be noticed that even if the numerical FSI model is overestimating the magnitude of experimental results in cases of both large TWA and TWS, it stays conservative and can therefore be considered as a safety factor in the industrial design context.

6. CONCLUSION

A robust method to solve nonlinear FSI yacht jib and mainsail has been presented in this paper. This study is part of an industrial project which aims to develop new designs of rigid sails of about 1000m² for cruise ships. A 50m² semi-rigid composite mainsail prototype has been built onshore on the Pornichet's dyke in France. The prototype is fitted with several sensors in order to study its mechanical behavior under aerodynamic loadings. The prototype has been modelled numerically to simulate the FSI on the structure. In this study, two types of comparisons were carried out in order to validate the FSI algorithm proposed here. The first type of comparisons deals with local comparisons between experimental measurements from the sensors and FSI results for a given TWA and TWS set. It has been shown that for local comparisons, the FSI algorithm is overall valid for all sensors as relative differences are less than 30%. The remaining differences can be partly explained by modelling and manufacturing discrepancies. The second type of comparisons is about global comparisons for three specific sensors and for a wide range of TWA and TWS. It was observed that for these global comparisons, the FSI algorithm is validated only for a specific range of TWA and TWS i.e. when $|TWA| < 10\,deg$ and $< 10\ \ kn$. Beyond these ranges, FSI results overestimate the magnitude of experimental measurements, but it can be seen as a safety factor for an industrial and conservative point of view. Moreover, dissimilarities might be explained by the fact that the dynamic effect of the structure was not considered in the FSI algorithm. Differences can also be explained by weather conditions during experimental campaigns. Indeed, during tests, the $[TWA, TWS]$ set was very unstable and therefore made it difficult to isolate stable and relevant time periods for comparisons. Future developments in order to improve FSI algorithm, should also model the jib's structure. In the light of these first results, the next consistent step related to the « Jib Sea » project is to perform FSI computations by using a viscous flow model. This will allow to better quantify the impact of using an inviscid flow model for the design stage of composite sails.

Acknowledgements

This study began in the "Solid Sail 2.0" project and now takes part in the "Jib Sea" project funded by the "Région Bretagne", and approved by the "Pôle EMC2" and the "Pôle Mer Bretagne Atlantique". This project involves a consortium of three industrial partners: "Chantiers de l'Atlantique", "GSea Design", "Multiplast" in collaboration with "ENSTA Bretagne" a graduate and post-graduate school of engineering as an academic partner. "Ocean Data System", subcontractor of "ENSTA Bretagne", has provided almost all components of the experimental setup for the mainsail. "Capacités SAS" carried out the instrumentation of the strain gauges. The authors gratefully acknowledge the four industrial partners for their technical support and collaboration and the Brittany region for its financial support.

Références

[1] S. Adanur, Wellington sears handbook of industrial textiles, CRC Press, 1995.

[2] I. Viola et R. Flay, «Sail aerodynamics: understanding pressure distributions on upwind sails,» *Experimental Thermal and Fluid Science*, vol. 35, n° %18, pp. 1497-1504, 2011.

[3] S. Bak et J. Yoo, «FSI analysis on a sail performance of a yacht with rig deformations,» *International Journal of Naval Architecture and Ocean Engineering*, vol. 11, n° %12, pp. 648-661, 2019.

[4] M. Sacher, H. Frédéric, P. Bot et M. Durand, «Sail trimming FSI simulation-comparison of viscous and inviscid flow models to optimise upwind sails trim,» *HPYD5*, 2015.

[5] M. Sacher, J.-B. Leroux, A. Nême et C. Jochum, «A fast and robust approach to compute nonlinear fluid-structure interactions on yachts sails - application to semi-rigid composite mainsail,» *Ocean Engineering*, vol. 201, pp. 107-139, 2020.

[6] L. Prandtl, «Theory of lifting surfaces. Technical Report. NASA,» 1920.

[7] J. Katz et A. Plotkin, Low-Speed Aerodynamics, Cambridge Aerospace Series 2nd edition: Cambridge University Press, 2001.

[8] E. Hairer, Norsett S.P. et G. Wanner, «Solving ordinary differential equations I: Nonstiff problems,» *Springer Science & Business Media*, vol. 8, 2008.

[9] Simulia, «Abaqus 2019 User's Manual,» 2019.

[10] D. Gay, Composite Materials : Design and Applications, 3rd éd., T. &. F. Group, Éd., CRC Press, 2015, pp. 263-285.

[11] A. Schiavi et A. Prato, «Non-linear stress relaxation of polymers: experimental evidences and stretched-exponential model,» chez *23rd International Congress on Sound & Vibration*, Athens, 2016.

[12] M. Sacher, H. Frédéric, R. Duvigneau , O. Le Maître, N. Aubin et M. Durand , «Efficient optimization procedure in non-linear fluid-structure interaction problem: Application to mainsail trimming in upwind conditions,» *Journal of Fluids and Structures*, vol. 69, pp. 209-231, 2017.